Machine Learning Designed and Experimentally Confirmed Enhanced Reflectance in Aperiodic Multilayer Structures

Prabudhya Roy Chowdhury, Krutarth Khot, Jiawei Song, Zihao He, David Kortge, Zherui Han, Peter Bermel, Haiyan Wang,* and Xiulin Ruan*

Machine learning (ML) methods have gained widespread attention in optimizing nanostructures for target transport properties and discovering unexpected physics. Here, an ML method is developed to discover and experimentally confirm binary CeO_2-MgO aperiodic multilayers (AMLs) for thermal barrier coatings with significantly enhanced reflectance. The effect of varying AML design parameters like total thickness, average period, and randomness in layer thicknesses, on the spectral and total reflectance is demonstrated. Introducing aperiodicity in layer thicknesses is shown to lead to a broadband increase in spectral reflectance due to photon localization. Since the number of possible AML structures increases exponentially with total thickness, a Genetic Algorithm optimizer is developed to efficiently discover AMLs with enhanced reflectance, for total thicknesses of 5–50 µm. Surprisingly, all the optimized structures show an odd number of layers with a CeO_2 layer at both ends, deviating from the traditional way of designing binary superlattices with paired layers. The optimized AML and a reference periodic superlattice of 5 µm thickness are fabricated by Pulsed Laser Deposition and characterized by optical reflectance measurements. The fabricated AML, despite considerable fabrication uncertainty, still enhances the reflectance to 48% from 40% of the reference superlattice, validating the effectiveness of our ML-based optimization process.

1. Introduction

The design of thermal barrier coatings (TBCs) for high temperature applications is extremely important in order to keep pace with the demand for higher efficiency operation of turbine engines and power generators. For example, although the efficiency of gas turbines can be increased by raising the turbine inlet temperature, this is severely limited by material considerations that provide an upper limit of temperature above which thermal degradation can occur. Thermal barrier coatings play a crucial role in preventing the turbine blades and rotors from reaching extremely high temperatures and mitigating the limitations imposed by the mechanical and thermal stability of the constituent materials. Since TBCs are responsible for retarding the transport of heat to the metallic turbine components, TBC materials are required to have low thermal conductivity and high melting points, which are commonly observed in ceramic materials such as yttria stabilized zirconia (YSZ).[1,2] In the past decades, significant efforts have been made to design improved TBC materials that can provide better thermal insulation at a lower coating thickness, which reduces the parasitic mass load for rotating turbine components. Heat transport to the metallic substrate through the TBC can take place via two pathways: heat conduction through phonons and thermal radiation through photons. At low temperatures, the heat transport is dominated by phonon mediated heat conduction and radiation effects are small. Consequently, much effort has been devoted to design materials and microstructures with low lattice thermal conductivity.[3–8] On the other hand, at higher temperatures, heat

P. Roy Chowdhury, K. Khot, Z. Han, X. Ruan
School of Mechanical Engineering and the Birck Nanotechnology Center
Purdue University
West Lafayette 47907, USA
E-mail: ruan@purdue.edu

J. Song
School of Materials Engineering
Purdue University
West Lafayette 47907, USA

Z. He, D. Kortge, P. Bermel
School of Electrical and Computer Engineering
Purdue University
West Lafayette 47907, USA

H. Wang
School of Materials Engineering
School of Electrical and Computer Engineering
Purdue University
West Lafayette 47907, USA
E-mail: hwang00@purdue.edu

transport by radiation can lead to a significant temperature increase of the metallic substrate, even as high as 50°C.[9] Significant insulation can be gained for better thermal management by mitigating radiative transport in the peak wavelengths of the incident irradiation, which is shifted to lower wavelength values at high temperatures according to the Wien's displacement law. For example, it has been shown that YSZ has a high transmittance to radiation in the wavelength of 0.3-5 µm,[10] which accounts for 90% of the total black-body irradiation at $T = 1500K$. As a result, TBC systems need to incorporate both phonon and photon scattering mechanisms for efficient thermal isolation at high temperatures. Similar to strategies for lowering lattice thermal conductivity by enhancing phonon scattering, several methods have been investigated to enhance photon scattering in TBCs for increased reflectance to the incoming thermal radiation. Wolfe et al.[11] studied the performance of $ZrO_2 - 8$ wt. % Y_2O_3 (8YSZ) whose microstructure was modulated by periodic strain fields, and found that the hemispherical reflectance was increased by 28–56%. One of the effective methods to reduce photon transmission is the use of multilayered and functionally graded TBCs. Such systems can overcome the limitations imposed by the thermophysical and optical properties of a single material, as well as enhance photon and phonon scattering at multiple interfaces within the system. Most studies in literature on such multilayered TBC systems have focused on the fabrication,[12,13] mechanical characterization,[14] and failure analysis.[12,13,15] Kelly et al.[16] reported a 73% infrared reflectance maximum at 1.85µm and an overall increase in reflection spectrum from 1–2.75µm in multilayer 7YSZ-Al$_2$O$_3$ TBC coatings. Huang et al.[17] designed and analyzed a system of similar constituent materials, where 7YSZ-Al$_2$O$_3$ multilayer stacks of varying layer thicknesses were used to achieve broadband photon scattering and high reflectance. Ge et al.[18] fabricated and studied the radiative transport properties of YSZ/NiCoCrAlY duplex TBCs and multilayered functionally graded TBCs with varying multilayer structures, porosities, and thicknesses. They found a negligible transmittance for the majority of YSZ/NiCoCrAlY functionally graded TBCs studied, with the top YSZ layer having a strong influence on the overall reflectance.

It is evident that multilayered TBC systems can exhibit superior performance in inhibiting both phonon and photon heat transfer. However, the process of development of such multilayered systems has largely been empirical and driven by experimental trial-and-error studies. Moreover, a large number of candidate materials and several design parameters such as individual layer thicknesses and stacking order of the constituent materials lead to a huge design space for multilayered TBC systems which cannot be efficiently searched using these traditional methods. In such problems, machine learning (ML) and materials informatics (MI) are very attractive and even indispensable tools in driving design optimization and discovering novel physical phenomena. ML and MI-based optimization methods, coupled with accurate yet expensive numerical simulations to evaluate candidate solutions, have been recently adopted to solve thermal transport engineering problems with great success, such as accelerating design of nanostructures with target thermal transport properties.[19–25] For example, a design optimization of $1 - D$ aperiodic superlattices (SLs) showing ultra-low lattice thermal conductivity was performed using a Bayesian Optimizer by Ju et al.[19] and using a Genetic Algorithm in one of our

previous works.[22] These studies have confirmed and further developed novel insights into the phonon transport mechanisms in these structures, including the role of phonon localization.[26] Probably more interestingly, machine learning has been used to successfully challenge conventional wisdom and discover exceptions in thermal transport.[24,25] MI methods have also been used to optimize nanostructure design for target radiative transport properties, notably for the design of selective emitters and reflectors for radiative cooling.[27–32] The great success achieved by ML and MI methods in the above studies encourages us to employ such methods for the design optimization of mutlilayered and functionally graded TBC systems.

In this work, we demonstrate the performance of CeO$_2$ and MgO-based periodic and aperiodic superlattice (SL) multilayer systems as high temperature TBCs with high reflectance to thermal radiation. Using a Genetic Algorithm (GA) optimization process, we are able to identify aperiodic multilayer (AML) structures with total thicknesses of 5–30µm that can reflect $\approx 60 - 93 \%$ of the blackbody radiation at $T = 1500K$. In this paper, we use the terms random multilayer (RML) and aperiodic multilayer (AML) interchangeably. The spectral reflectance and transmittance of each candidate structure is calculated using the transfer matrix method. First, we calculate the reflectance of periodic CeO$_2$-MgO SLs with varying total and average layer thicknesses, and identify the occurrence of an optimal average layer thickness at which the total reflectance is maximized. The effect of having aperiodic layer thicknesses on the reflectance is studied by manually providing varying degrees of perturbation to the individual layer thicknesses, which causes localization of photons. Next, we employ our GA based optimization process on multilayer systems with total thickness varying from 5–30µm. The GA-optimized structures show a broadband high reflectance in the wavelengths coinciding with the peak blackbody radiation at the desired temperature. In order to validate our robust ML-based discovery approach of high reflectance AML structures, we fabricate the optimized AML and reference SL with 5µm total thickness using Pulsed Laser Deposition, and the optical performance of these structures are characterized by optical reflectance measurements. The optimized structures show a significant increase in reflectance due to non-intuitive structural features such as the presence of an unpaired CeO$_2$ interface at the end as well as an optimal layer thickness distribution throughout the AML.

2. Experimental Section

2.1. Simulation Methods

2.1.1. Transfer Matrix Method for Calculating Reflectance of Multilayer Structures

The reflectance and transmittance of a 1D multilayer structure was evaluated using the transfer matrix method, which solves the Maxwell's equations subject to a uniform normal electric field **E**. The interfaces between CeO$_2$ and MgO layers were assumed to be perfectly smooth. Within the multilayer system, the field E_i is composed of its forward (transmitted) component E_i^+ and its backward (reflected) component E_i^-. The schematic of the multilayer system with the field components is shown in **Figure 1a**. It uses the convention of naming the fields at the left end of each
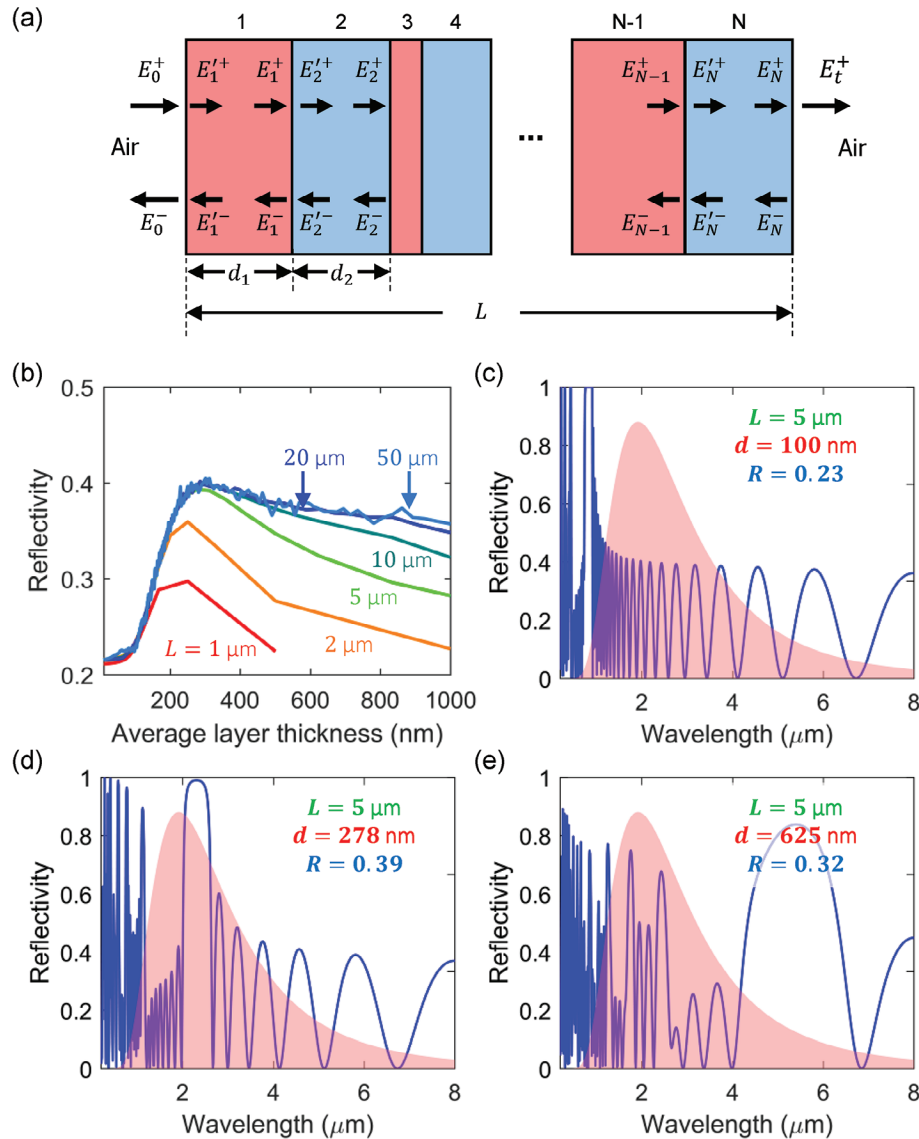
Figure 1. a) Schematic of multilayer structure with N layers showing the transmitted and electric field components calculated in the TM method (b) Variation of total reflectance with average layer thickness for CeO_2-MgO periodic superlattice (SL) structures for total thicknesses of 1–50 μm. The spectral reflectance versus wavelength is shown for three different structures with total thickness of 5 μm and average layer thickness of (c) d_{avg}=100nm, (d) d_{avg}=278nm which gives the highest reflectance among SLs with total thickness of 5 μm, and (e) d_{avg}=625nm. The shaded plot in the background represents the shape of the blackbody thermal radiation spectrum at T=1500K.

layer as $E_i'^+$ and $E_i'^-$ and those at the right end as E_i^+ and E_i^-. The field components on each end of a layer of material A, with complex refractive index m_A, are related by:

$$\begin{bmatrix} E_1'^+ \\ E_1'^- \end{bmatrix} = \begin{bmatrix} e^{ik_A(d_A)_1} & 0 \\ 0 & e^{-ik_A(d_A)_1} \end{bmatrix} \begin{bmatrix} E_1^+ \\ E_1^- \end{bmatrix} = (\mathbf{P_A})_1 \begin{bmatrix} E_1^+ \\ E_1^- \end{bmatrix} \quad (1)$$

here, $(d_A)_1$ is the thickness of the 1st layer composed of material A (as an example), $k_A = 2\pi m_A/\lambda_0$ is the wave number, λ_0 is the wavelength in vacuum, and m_a and m_b are the complex refractive indices of the two materials A and B, respectively. In this work, the refractive indices of MgO measured by Stephens and Malitson[33] for the wavelengths of 0.36–5.35 μm, and those of

CeO$_2$ measured for wavelengths of 0.25–1.09 μm by Gue et al.[34] were used. The refractive index at higher wavelengths till 8 μm were obtained using a simple linear extrapolation.

From Equation (1), the field components on either side are related as

$$\begin{bmatrix} E_1^+ \\ E_1^- \end{bmatrix} = \begin{bmatrix} \frac{m_B+m_A}{2m_A} & \frac{m_B-m_A}{2m_A} \\ \frac{m_B-m_A}{2m_A} & \frac{m_B+m_A}{2m_A} \end{bmatrix} \begin{bmatrix} E_2'^+ \\ E_2'^- \end{bmatrix} = \mathbf{I_{12}} \begin{bmatrix} E_2'^+ \\ E_2'^- \end{bmatrix} \quad (2)$$

Equations (1) and (2) can be written for all N layers in a multilayer system, and the field components at the boundaries of the

multilayer can be related using the equation:

$$\begin{bmatrix} E_0^+ \\ E_0^- \end{bmatrix} = \mathbf{I}_{01}(\mathbf{P_A})_1\mathbf{I}_{12}(\mathbf{P_B})_2\mathbf{I}_{23} \dots \mathbf{P_N}\mathbf{I}_{N(N+1)} \begin{bmatrix} E_t^+ \\ 0 \end{bmatrix} \quad (3)$$

For a given value of the incident field E_0^+, Equation (3) may be solved for the reflected field component E_0^- and the transmitted field component E_t^+. One can then obtain the spectral reflection and transmission coefficients from the relations:

$$R(\lambda) = |\frac{E_0^-}{E_0^+}|^2 \quad (4)$$

$$T(\lambda) = |\frac{E_t^+}{E_0^+}|^2 \quad (5)$$

In order to evaluate the relative performance of the different multilayer structures in high temperature TBC applications, the total reflectance was calculated by integrating the spectral reflectance weighted by the blackbody radiation spectrum at 1500K. While the spectral properties could provide insight into the physical behavior of these systems, the integrated total reflectance value could be used as an objective function while optimizing the multilayer structures for best performance. The total reflectance is calculated as:

$$R_{total} = \frac{\int R(\lambda)G_{bb}(\lambda, T = 1500)d\lambda}{\int G_{bb}(\lambda, T = 1500)d\lambda} \quad (6)$$

where the blackbody radiation G_{bb} at a temperature T is given by:

$$G_{bb}(\lambda, T) = \frac{2\pi hc^2}{\lambda^5} \frac{1}{e^{\frac{hc}{k_B\lambda T}} - 1} \quad (7)$$

here, h is the Planck constant, c is the speed of light in vacuum and k_B is the Boltzmann constant.

2.1.2. Genetic Algorithm Optimization Framework

In order to find the random multilayer configuration with the highest reflectance, a Genetic Algorithm (GA) optimizer was developed, which was an evolutionary algorithm that mimics the principle of natural selection to find the optimal solution. Since the GA is not a gradient-dependent optimization process, it works well for problems involving a complex response surface since the GA can avoid getting trapped within a region of local optimum. Moreover, GA's have been found to have superior performance compared to other gradient-based optimization problems when the number of optimization variables is large, and candidate evaluations within each iteration can be parallelized to reduce computational time. In a GA based optimization, candidate solutions within the design space are encoded as individuals or phenotypes with properties represented as chromosome strings that are altered by evolutionary operations. The GA was started with an initial population of encoded individuals that might be chosen randomly or using any prior knowledge available about the design space. In each iteration or generation, the individuals in the population were evaluated with respect to a suitably

designed objective function, and a fitness value was assigned to the individual based on this evaluation. In the next step, a new population of parents was formed by probabilistic selection from the current generation, where individuals with high fitness value had a higher probability of being selected. This step ensures that only the best properties or genes in each generation are propagated to the next generation, thus leading the generation toward better fitness individuals. Subsequently, the evolutionary operations of crossover and mutation were performed to breed a new generation from the selected population of high-fitness parents. Crossover was performed by choosing a pair of individuals from the parent pool and stochastically combining genes from these parents to form two new offsprings. On the other hand, mutation introduced genetic diversity in a single offspring by altering the value of one or more randomly selected genes that could introduce candidate solutions from unexplored regions of the design space. Both these operations were performed with a probability of occurrence that needs to be suitably chosen to ensure a balance between exploration of new solutions and exploitation of already explored solutions. A new generation of candidate solutions was obtained after performing the operations of selection, crossover, and mutation, which is then progressed to the next iteration of the GA. To stop the GA, a convergence criteria could be set such as a target fitness value or a relative change in fitness value over several successive generations.

In this work, the periodic and random superlattices were encoded as N-bit binary arrays, where each bit in the array represents the type of material for a 10 nm thick layer at the corresponding position along the length of the superlattice. Each bit in the array was encoded as *one* if the corresponding position consists of a CeO_2 layer or *two* if it consisted of a MgO layer. Thus, design space consisted of 2^N possible solutions for a superlattice system of $10 \times N$ nm total thickness. A population size of 1000 was chosen for all thicknesses studied. Since the aim was to identify the multilayer structure with the highest reflectance, the objective function was chosen as the total reflectance calculated using the transfer matrix method. The initial generation was populated by randomly generating superlattice structures while also covering the entire range of possible average layer thicknesses. A rank-based selection process was implemented, where the probability of an individual to be selected as for the parent pool was inversely proportional to the rank of the individual when the entire population was sorted in decreasing order of the objective function. The probability of selection is given by the expression

$$P(i) \propto \frac{1}{c + rank(i)} \quad (8)$$

where c is a parameter than can be adjusted to control the selectivity of best-fit individuals. The probabilities were normalized such that the sum of all probabilities was one. After selection of the parent pool, crossover, and mutation were performed 80% and 50% of the time. A single-point crossover was used, in which a random position was chosen along the N-bit binary arrays of two parents and the sections of the arrays succeeding the chosen position were interchanged between the two parents to form the two new offspring. The mutation operation was performed in either of two ways, which could occur with equal probability: i) a single bit was chosen along the N-bit array of the offspring, and its
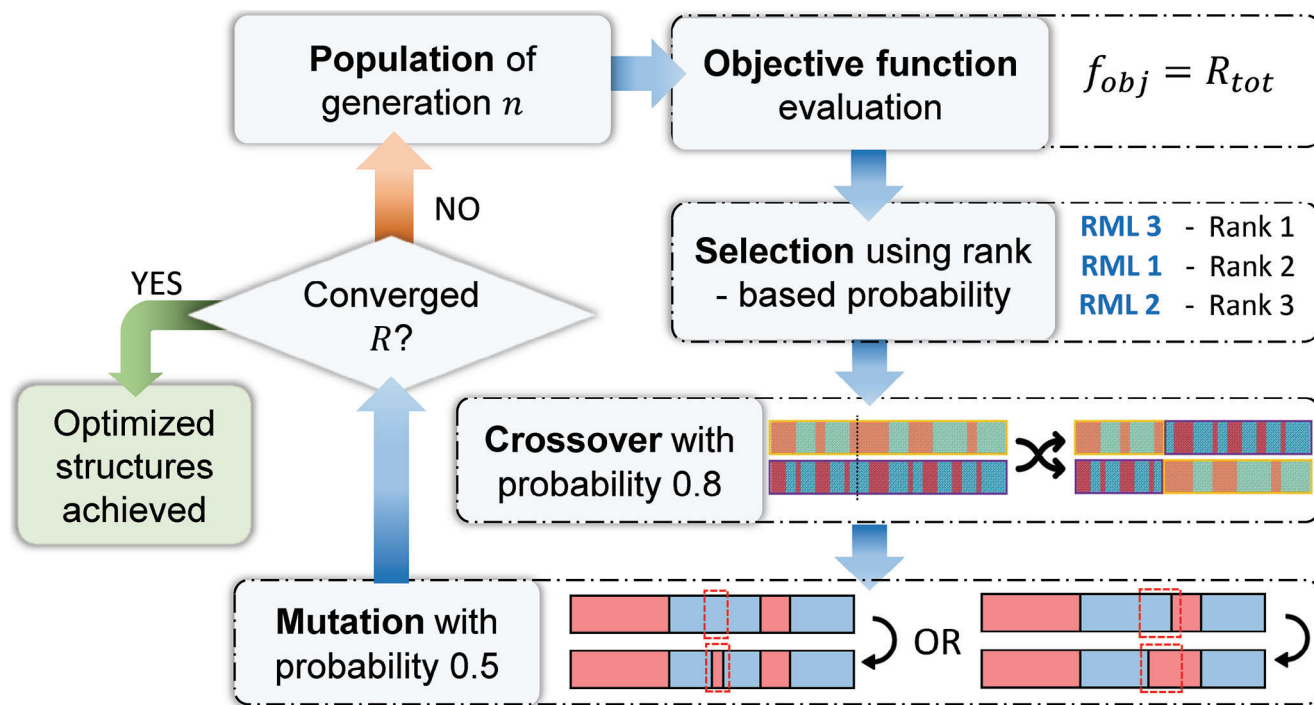
**ADVANCED
SCIENCE NEWS**

www.advancedsciencenews.com

**ADVANCED
OPTICAL
MATERIALS**

www.advopticalmat.de

Figure 2. a) Schematic of the Genetic Algorithm (GA) based optimization process, showing the implementation of the selection, crossover, and mutation steps.

value of the variable was flipped (1 to 2 or vice-versa) to change the material occurring at that location, or ii) a random layer (group of bits with the same value) was chosen and its length was increased or decreased randomly (the length of the adjacent layer was decreased or increased correspondingly to ensure the total thickness of the structure was preserved). The first method of mutation serves to perturb the number of interfaces in the structure, while the second method provides random perturbations to the layer thicknesses. **Figure 2** provides a schematic of the GA optimization process, including the implementation of selection, crossover, and mutation operations.

2.2. Experimental Methods

2.2.1. Sample Preparation

The CeO_2-MgO films with periodic and random multilayer structures were deposited on MgO (100) substrates using pulsed laser deposition (PLD) (with a KrF excimer laser, Lambda Physik Compex Pro 205, $\lambda = 248$ nm). The layered structures were formed by alternative ablation of CeO_2 and MgO targets. The thickness of each layer was controlled by the number of laser pulses based on the growth rate of CeO_2 and MgO. The chamber pressure was lower than 1×10^{-6} mTorr before deposition and a 20 mTorr oxygen pressure was maintained during deposition. The deposition temperature was kept at 600 °C and the chamber was cooled down to room temperature under 20 mTorr O_2 after deposition.

2.2.2. Microstructure Characterization

X-ray diffraction (XRD, PANalytical Empyrean with Cu Kα1 radiation) was used to characterize the crystallinity of the as-

deposited specimens. High-angle annular dark field scanning transmission electron microscopy (HAADF-STEM) and energy-dispersive X-ray spectroscopy (EDS) were conducted on Thermo Fisher Scientific Talos F200X TEM to compare the microstructures of the periodic and random multilayer structures. The cross-sectional TEM specimens were prepared using focused ion beam (FIB, FEI quanta 3D FEG) milling.

2.2.3. Optical Characterization

The optical measurement in the UV–vis NIR range was performed using Perkin-Elmer 950 UV–vis-NIR spectrometer with an integrating sphere. The transmittance measurements were done for a range of 0.25 to 2.5 μm . The transmittivity was converted to reflectance by assuming the sum of the two quantities equals one, assuming there was no absorption. The Fourier transformed infrared spectroscopy (FTIR) measurement was done using Nexus 670 spectrometer covering wavelengths from 2 to 10 μm. The FTIR instrument composed of a Michelson interferometer combined with a mercury cadmium telluride (MCT) detector. These two measurements were compiled together to make the final analysis and calculation of total reflectance.

3. Results

3.1. Reflectance of Periodic Multilayer Structures

In this work, multilayer structures composed of CeO_2 and MgO are chosen due to the large contrast in their refractive indices as well as their high melting points which are crucial for thermal

**ADVANCED
SCIENCE NEWS**

www.advancedsciencenews.com

**ADVANCED
OPTICAL
MATERIALS**

www.advopticalmat.de

stability in high temperature TBC applications. A schematic of a multilayer structure with N layers is shown in Figure 1a. The layer thicknesses may be periodically alternating to form a superlattice (SL) or may be randomly chosen to form a random multilayer (RML). The total thickness of the systems studied in this work range from 5–50 μm and the shortest thickness of each individual layer is allowed to be 10 nm.

We first evaluate the reflectance of CeO$_2$-MgO based periodic superlattice multilayer structures using the transfer matrix method (TMM) which is described in the Experimental Section. The main design variables that can be optimized in periodic SLs are the total thickness L and the repeating layer thicknesses d_{CeO_2} and d_{MgO}. Figure 1b shows the total reflectance of SLs with equal layer thicknesses of CeO$_2$ and MgO, where we vary the total thickness from 1–50 μm and individual layer thickness from 10 nm–1 μm. The plots for each total thickness show a similar trend where the total reflectance initially increases with the average layer thickness and eventually reaches a peak reflectance value, following which a decrease in reflectance is observed. To understand the reason behind this trend, we compared the spectral reflectance of SLs with total thickness of 5 μm and three different average layer thicknesses as shown in Figure 1c–e. In all three cases, we observe the existence of strong oscillations in the spectral reflectance, obtained from constructive and destructive interference due to multiple phase-preserved reflections at the different interfaces in the multilayer structure. We also notice the existence of a high reflectance photonic "stopband" in each of the structures, which is similar to that observed in a distributed Bragg reflector. The wavelength at which this stopband occurs is found to vary with the average layer thickness of the structure, and coincides with the location of the peak blackbody thermal radiation spectrum (shown by the shaded plot in the background) at an average SL layer thickness of 278 nm, causing the peak reflectance to occur at this layer thickness.

The total reflectance of SLs with a fixed average layer thickness also shows an initially increasing trend with increasing total thickness of the system. This can be seen in Figure 1b, where the reflectance at a constant average layer thickness increases from $L = 1$ μm to $L = 20$ μm. For higher total thicknesses, the reflectance does not show an increasing trend, and can even decrease slightly, as evident from the lines corresponding to $L = 20$ μm and $L = 50$ μm. Moreover, the increase in reflectance with increasing total thickness is more significant at average layer thicknesses greater than ~200 nm. The trend of increasing reflectance with increasing total thickness at these average periods can be attributed to the higher number of interfaces within the SL at larger thicknesses, leading to more repeated reflections.

3.2. Reflectance of Random Multilayer Structures

Next, we analyze the effect of introducing randomness in the individual layer thicknesses on the reflectance of periodic superlattice structures. In providing such randomness to the SL layer thicknesses, we ensure that the total multilayer thickness, as well as the total thickness of each constituent material are conserved to ensure a fair comparison. In order to quantify the degree of randomness in a random multilayer structure, we use the standard deviation of the layer thickness perturbations as a percentage of average layer thickness, which is calculated as:

$$\delta = \frac{1}{d_{avg}} \sqrt{\frac{\sum_{i=1}^{N} (\Delta_i - \bar{\Delta})^2}{N - 1}} \tag{9}$$

where, Δ_i is the deviation of the ith layer thickness of the N-layer RML from the corresponding SL layer thickness, and $\bar{\Delta} = 0$ for conservation of total thickness of the constituent materials. Such a definition of degree of randomness does not uniquely specify a RML structure, since the relative positions of the layers does not affect δ at all. As a result, there may still be significant variation of reflectance among structures with the same total thickness, average layer thickness and degree of randomness. To account for this, we generate three independent random structures at each average layer thickness and degree of randomness, and choose the maximum total reflectance value among the three RMLs for the corresponding data point.

Figures 3a,b shows the effect of randomization of superlattice layer thicknesses on the total reflectance for two total thicknesses of 5 μm and 50 μm, respectively. For both cases, the total reflectance is found to increase with increasing degree of randomness up to $\delta \approx 40\%$, after which a non-monotonic fluctuation is observed. While the maximum reflectance observed in the periodic structure without randomness is 0.39 and 0.41 for 5 μm and 50 μm thick superlattices, respectively, the addition of randomness can increase the reflectance to 0.50 and 0.90. The spectral reflectance is compared between a periodic and random structure (with $\delta = 40\%$) for 5 and 50 μm total thicknesses in Figure 3c,–f, respectively. It can be seen that the randomization of layer thicknesses causes an overall broadband increase of the reflectance peaks, implying a low transmission in these structures. This effect can be attributed to the randomness-induced localization of photons, similar to Anderson localization of electrons,[35] and has been studied theoretically and experimentally in similar $1 - D$ disordered systems.[36–38] The phase-preserved reflections occurring at the randomly distributed interfaces within the RML can cause constructive and destructive interference in a manner that the field is enhanced in and confined to certain finite spatial regions.

3.3. Genetic Algorithm Based Optimization of RMLs with High Reflectance

As mentioned previously, for a fixed total thickness, average layer thickness and degree of randomness, there may exist a large number of possible solutions of individual layer thicknesses and their spatial distributions, each leading to a different "realization" of a RML structure. Considering a smallest allowable individual layer thickness of 10 nm, the number of possible RML structures for a total thickness of L μm is 2^{100L}. With increase in the total thickness of the structure, the size of the design space containing all possible realizations increases exponentially, and cannot be covered by an exhaustive search or even an intuition-guided optimization process. Moreover, our simulation results on a small number of realizations show that a significant variation in total reflectance can exist within structures having the same total
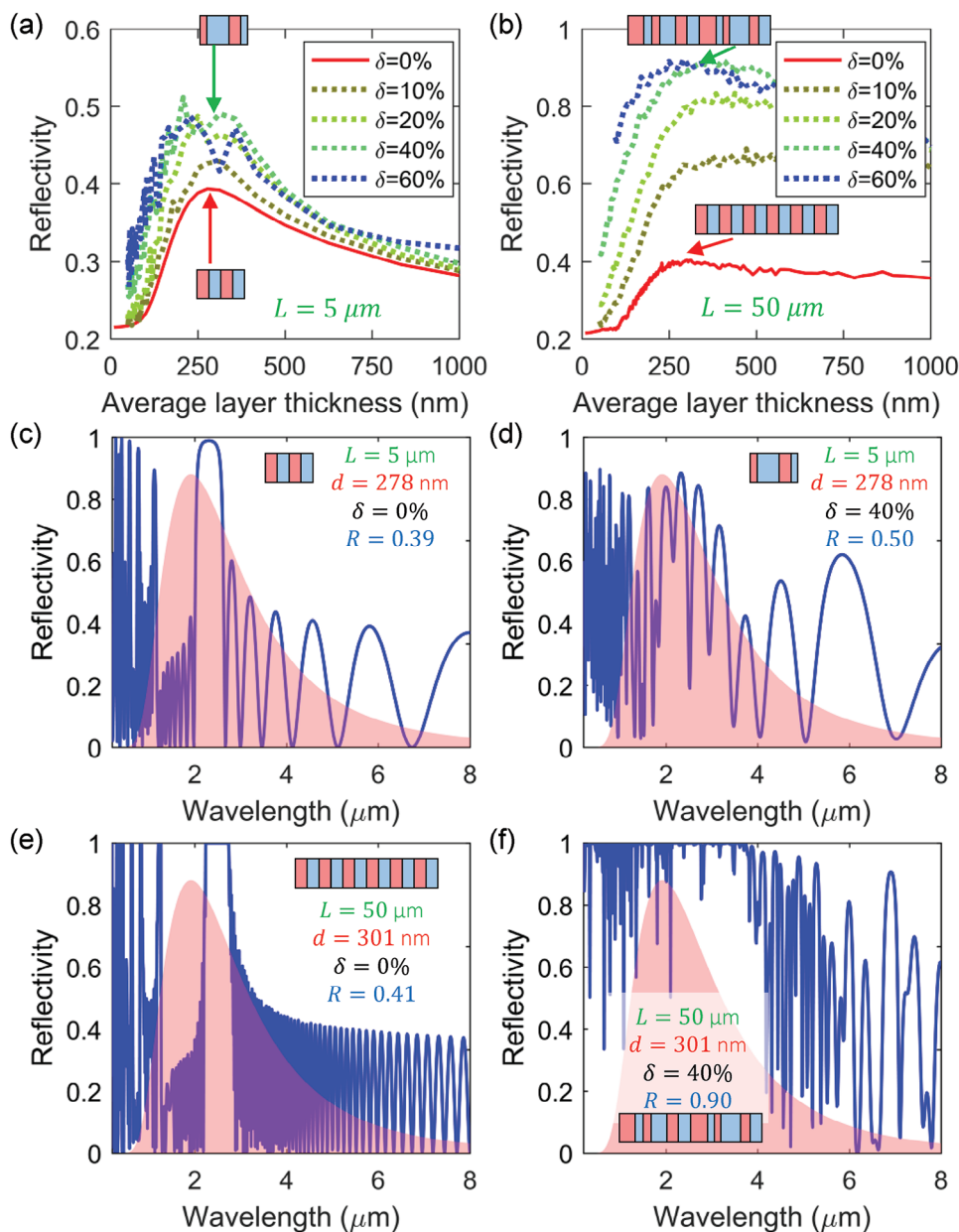
**ADVANCED
SCIENCE NEWS**

www.advancedsciencenews.com

**ADVANCED
OPTICAL
MATERIALS**

www.advopticalmat.de

Figure 3. Total reflectance versus average layer thickness, showing the effect of randomizing the superlattice layer thicknesses by $\delta = 10, 20, 40$, and 60%, for two total thicknesses of (a) $L = 5\mu m$ and (b) $L = 50\mu m$. The spectral reflectance versus wavelength is plotted for comparison between two 5μm structures with (c) $\delta = 0\%$ (perfectly periodic) and (d) $\delta = 40\%$; and for two 50μm structures with (e) $\delta = 0\%$ (perfectly periodic) and (d) $\delta = 40\%$. The shaded plot in the background represents the shape of the blackbody thermal radiation spectrum at $T = 1500K$. (Inset multilayer structures are for visual aid only and do not represent the actual structures).

thickness, average layer thickness, and degree of randomness. It is evident that in order to efficiently scan the design space for high reflectance RML structures with a target total thickness, an alternative approach such as an automated and data-driven optimization method is necessary.

Here, we use a Genetic Algorithm (GA) based automated optimization framework to identify the RML structure with highest reflectance. The details of the GA framework are outlined in the Experimental Section, and the results of the optimization process are provided here. **Figure 4a** shows the evolution of the

maximum reflectance among all structures in each generation of the GA optimization, for the total thicknesses of 5, 10, 20, 30, and 50 μm. In each case, the initial population contained RML structures with a large range of average layer thicknesses in order to promote sufficient diversity among the individuals and remove any inherent bias to the optimization process. For each run, the maximum reflectance is observed to increase from an initially low value, corresponding to the expected reflectance obtained if an RML was randomly generated, and converge to a much higher reflectance after a number of generations. The maximum
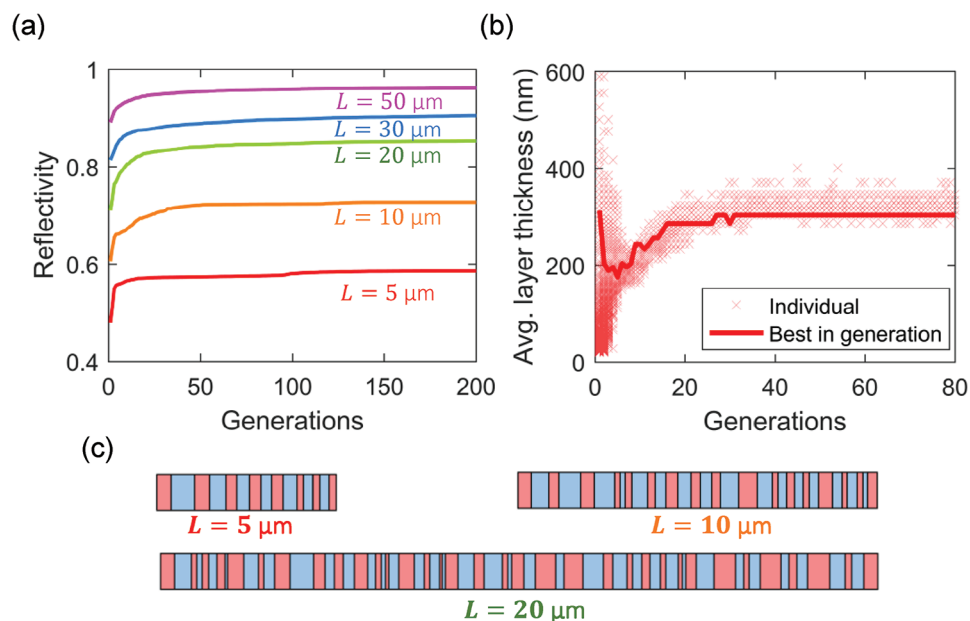
**ADVANCED
SCIENCE NEWS**

www.advancedsciencenews.com

**ADVANCED
OPTICAL
MATERIALS**

www.advopticalmat.de

Figure 4. a) Evolution of maximum reflectance identified by the genetic algorithm (GA) optimizer vs. generation of optimization, for four different total thicknesses of 5, 10, 20, 30, and 50 μm b) The average layer thicknesses of all individuals in the population (red crosses) at each generation of the GA optimization run for a total thickness of 10μm. The solid line shows the average layer thickness of the RML with highest reflectance at each generation of the optimization process. c) Design of the GA-optimized RML structures with high reflectance for three total thicknesses of 5, 10, and 20 μm.

reflectance obtained in the optimized structures is 58.6%, 72.6%, 85.5%, 90.0%, and 96.9% for total thicknesses of 5, 10, 20, 30, and 50 μm, respectively, which translates to an enhancement of 22.0%, 19.7%, 20.5%, 11.8%, and 8.7% over that obtained in randomly generated RML structures of the same total thicknesses. As shown in Figure 4b for the case of an optimization run on a system with total thickness of 10 μm, the GA optimizer searches through structures with various average layer thicknesses and finally converges to a value of 303 nm, which is found to provide the structure with the highest reflectance. The average layer thicknesses of the GA optimized structures for all total thicknesses studied are found to lie in the range of $290-350$ nm.

The designs of the GA-optimized RML structures for different total thicknesses are shown in Figure 4c. A notable feature observed in all the optimized structures is the presence of a CeO_2 layer at both ends of the RML, leading to an odd number of layers within the RML. This is in contrast to the traditional method of superlattice design, where the layers are usually paired and the structure contains an even number of layers. Since CeO_2 provides a higher contrast in refractive index to air than MgO, the presence of a CeO_2 layer at either end of the structure results in an interface with a higher reflection coefficient leading to enhancement of the total reflectance. This surprising feature of an odd number of layers in a binary superlattice has been previously demonstrated in thermophotovoltaics (TPV) design,[39] but has not been applied to superlattice structures with tailored thermal transport properties.

To gain further insight into the superior performance of the GA-optimized RML structures, we compare the spectral reflectance of three different structures as shown in **Figure 5a–c**: the GA-optimized RML with a total thickness of 10 μm, the reference periodic SL structure with same total thickness and average

layer thickness, and a non-optimized RML, which was randomly generated from this reference SL structure using a degree of randomness $\delta = 40\%$. As can be observed in the figures, the inclusion of randomness causes an increase in the reflectance peaks in a wide range of wavelengths from the reference periodic SL. However, the wavelengths of the high reflectance peaks in the GA-optimized structure coincide with the location of the peak blackbody radiation spectrum at $T = 1500 K$ (shown by the shaded plot in Figure 5a–c). As a result, the integrated total reflectance of the GA-optimized structure is higher than that of the periodic SL, which shows an overall lower spectral reflectance, as well as the non-optimized RML for which the high reflectance peaks do not coincide with the location of peak blackbody radiation.

The variation of the reflectances of the ML-explored RML structures with respect to the average layer thickness is shown in **Figure 6a** for the structures with a total thickness of 5 μm. The reflectances of the periodic SLs with same thickness is also shown in the figure for reference. We observe that the peak RML reflectance is observed at an average layer thickness of ≈ 330 nm, which is different than that at which the peak SL reflectance is observed (≈ 290nm). This demonstrates that without using an ML search method, it would not have been possible to arrive at the best RML structure by following the intuitive direction of providing randomness to the best SL structure. We also compared our optimized RML structures with a Quarter Wavelength Multilayer structure and a Distributed Bragg Reflector (DBR) multilayer structure. DBRs can provide a high reflectance within a "forbidden" wavelength band by designing the layer thickness to be $1/4^{th}$ of the wavelength of this photonic stopband. In the first structure, both alternating layers are equal to $1/4^{th}$ of the peak wavelength (≈ 2 μm) (Quarter Wavelength Multilayer in Figure 6a), while in the second structure, the alternating layer

**ADVANCED
SCIENCE NEWS**

www.advancedsciencenews.com

**ADVANCED
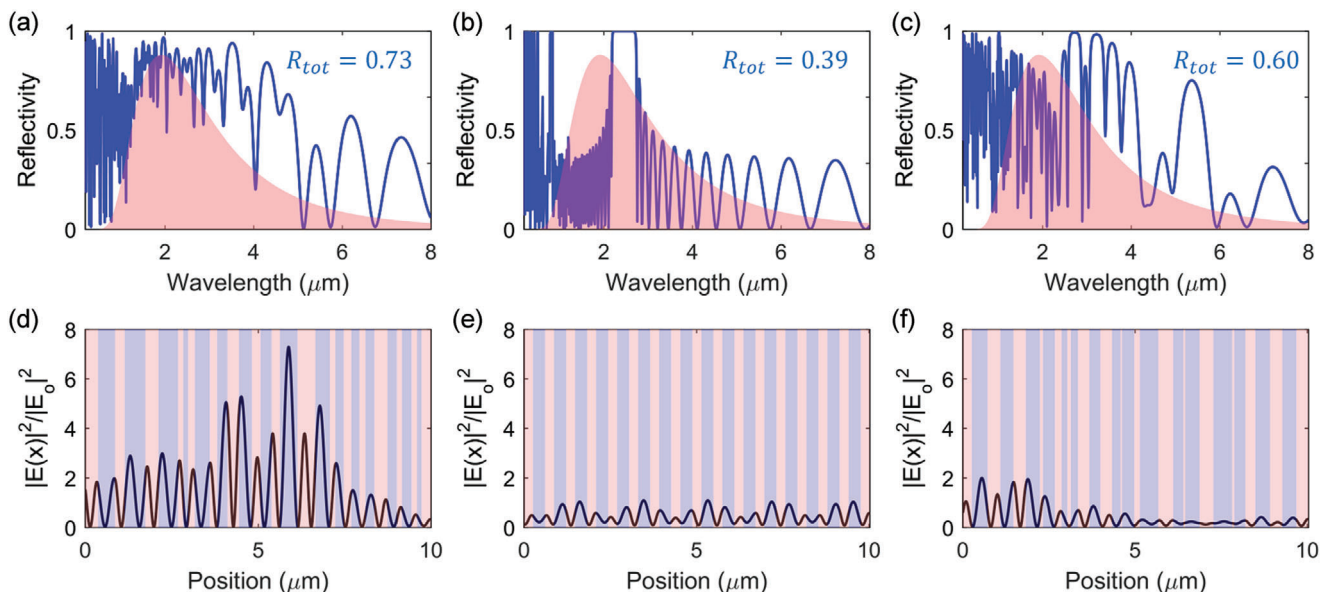OPTICAL
MATERIALS**

www.advopticalmat.de

Figure 5. Spectral reflectance versus wavelength for three multilayer structures with total thickness of 10 μm: a) GA-optimized RML with high reflectance, b) periodic SL with same average layer thickness, and c) a non-optimized RML structure with same average layer thickness. The field intensity distribution versus position along the multilayer structure is shown for the same structures for a wavelength of 1.84 μm: d) GA-optimized RML with high reflectance, showing significant field enhancement, e) periodic SL with same average layer thickness, and f) a non-optimized RML structure with same average layer thickness. The *x*-direction denotes the stacking direction of the multilayer structures.

thickness of material i with refractive index n_i is calculated according to the formula $d_i = 2\mu m/(4 \times n_i)$ (DBR in Figure 6a). As observed in the figure, the optimized RML shows a much higher reflectance than both the multilayer and the DBR structures.

As mentioned in the previous section (Figure 3), during the manual search, we observed a non-monotonic variation of reflectance of the superlattice structures with increasing degree of randomness. Following the GA-based search process, we plot the reflectance of the explored structures with respect to the calculated degree of randomness of each structure (as defined by Equation (9)) in Figure 6b. Due to the vast number of structures explored, we have only plotted the best structured identified in each iteration of the search. As observed in the plot for two total thicknesses of 5 and 20 μm, the reflectance initially increases with increasing degree of randomness to a maximum reflectance reached at 40% randomness for 5 μm thickness and 50% randomness for 20 μm. Following this maximum, the reflectance is found to decrease with further increase of degree of randomness. We attribute this non-intuitive trend of an initial increase and subsequent decrease of reflectance with increasing randomness in layer thicknesses to the following reasons. At a low degree of randomness, the photon transport is largely coherent due to the low rate of randomness-induced photon scattering. In this regime, an increasing degree of randomness causes higher coherent photon localization and leads to a higher reflectance. The impact of this coherent photon localization keeps on increasing till a critical degree of randomness is reached, following which the photon transport starts to become dominated by incoherent photon scattering. As we keep on increasing the degree of randomness beyond this point, the impact of coherent photon transport and localization diminishes. This leads to a lower reflectance than that observed at the critical degree of randomness.

To elucidate the effect of photon localization on the enhanced reflectance in the GA-optimized RML structure, we also calculate the distribution of field intensity inside the above multilayer structures. The magnitude of the local field at any position x along the direction of the multilayer structure can be obtained from the sum of the forward and backward components as:

$$|E(x)| = |E^+(x) + E^-(x)| \tag{10}$$

The normalized field intensity at any position can then be calculated as $|E(x)|^2/|E_0|^2$, which is shown in Figure 5d–f for a representative wavelength of 1.84 μm. Our results show a significant field enhancement within certain spatial regions within the GA-optimized RML structure, which is lower in the non-optimized RML structure and largely absent in the periodic SL structure. This clearly demonstrates the presence of photon localization within the optimized RML structures leading to high reflectance.

3.4. Experimental Realization and Reflectance Measurements

Following the GA-based optimization process, it is important to experimental confirm the results of enhanced reflectance in our optimized RML structures. In this work, we used Pulsed Laser Deposition (PLD) to fabricate the GA-optimized RML and the reference periodic SL structures with a total thickness of 5 μm. The details of the fabrication and characterization process are elaborated in Experimental Section, and the schematics of the two structures are shown in **Figure 7a,d**. Figure 7b,e show the the TEM images for the cross-section of the two structures, while the EDS images are shown in Figure 7c,f. Both the deposited multilayer structures have smooth and well-defined interfaces, which
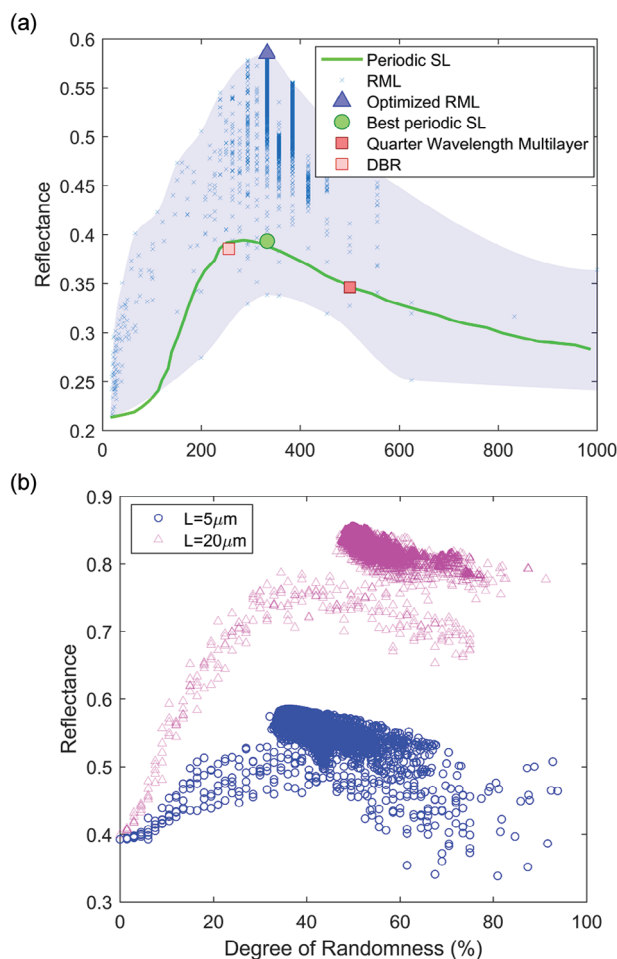
Figure 6. a) Reflectance of the ML-exlored 5μm thickness multilayer structures versus average layer thickness (blue crosses), with the optimized RML shown by the triangle. The green lines shows the reflectance of periodic structures with the same thickness, and the circle shows the best periodic superlattice with same mass ratio as the optimized RML. The reflectances of a Quarter Wavelength Multilayer and a Distributed Bragg Reflector (DBR) are shown for comparison. b) Reflectance of the ML-explored multilayer structures versus the Degree of Randomness, for total thicknesses of 5 and 20 μm.

Table 1. Designed and Fabricated (exp.) thicknesses in μm of the optimized RML and reference periodic SL

RML (design)	200	260	190	260	180	390	320	300	320	350	300	460	420	650	400
RML (exp.)	201	524	189	515	174	789	309	614	318	717	286	905	382	1291	376
SL (design)	291	381	291	381	291	381	291	381	291	381	291	381	291	381	291
SL (exp.)	227	363	229	369	229	362	229	380	246	383	246	387	236	383	270

is necessary for their optical performance. **Table 1** shows the layer thicknesses of the designed and fabricated RML and SL structures. We note that there are some deviations from the target layer thicknesses due to the uncertainty of the fabrication process and limitations of the equipment. We measured a total thickness of 4.5 μm for the periodic multilayer and a thickness of 7.5 μm in the fabricated RML. Moreover, the XRD characterization shown in Figure 7g indicates that both the structure are crystalline and

stable. It is noted that the film thicknesses are not exactly the same as the predicted multilayer structures. This is due to the processing challenges in using pulsed laser deposition method for the multilayer growth. First, the growth rate is relatively low which results in the very long depositions. To complete the entire 5 μm film, 3 runs were applied for this deposition. Second, because of the long runs, significant target surface modification also results in the modified growth rates across the multiple runs for the thick multilayer films. These also lead to the variation in the final film thickness.

The transfer matrix method was used to calculate the reflectance of the fabricated multilayer structures. To understand the impact of deviation from the target layer thicknesses in the fabricated structures, we perform the calculation for two layer thickness configurations in each case - the design thicknesses (GA-generated layer thicknesses) and the fabricated thicknesses (measured layer thicknesses of the fabricated structures). The TMM simulated reflectance spectra of the two thickness configurations are shown in **Figure 8a** for the RML and Figure 8b for the periodic SL. In both cases, the spectral reflectance for these two thickness configurations were found to be very similar, implying minimal impact of fabrication uncertainty related layer thickness deviation. The simulated reflectance using fabricated thickness for the RML shows a slightly higher reflectance for longer wavelengths in Figure 8a, possibly due to large total thickness and some large layers included in the system. On the other hand, the simulated reflectance using fabricated thicknesses for the periodic SL shows a slightly shifted location of the maximum reflectance peak compared to the design thickness structure in Figure 8b, which is due to the different average period in the fabricated structure.

The above simulations are also compared with measurements of reflectance spectra in UV–vis–NIR and FTIR spectrum. Figure 8a,b demonstrate a good overall agreement between the simulated and measured reflectance spectra for both multilayer structures, with features such as the major peaks and valleys in the simulated spectra being well-represented in the measured data. Notably, we observe that in both the simulated and measured reflectance spectra, the single high reflectance peak in the periodic SL is replaced by an overall broad-spectrum enhanced reflectance in the RML structure. Once again, we observe a small shift in the location of the maximum reflectance peak between the simulated spectra using fabricated thicknesses and the measured spectra for the periodic SL in Figure 8b. This indicates a further difference of average period thickness in the fabricated structure, which can be explained by the fact that the PLD deposited structures show a variation in layer thicknesses from the center to the edges of the structures. This leads to a shift in average period thickness that cannot be captured in our TMM simulations. This deviation of the reflectance spectra due to non-ideal layer thicknesses was previously also noted by Huang et al.[40] Moreover, the presence of other non-ideal effects such as grain boundaries, crystallinity, and defects in the fabricated structures cause further mismatch of the simulated and experimental optical spectra.

To compare the performance between the two fabricated multilayer structures (optimized RML and SL), we calculate their total reflectance as shown in Figure 8c. The GA-optimized RML shows a higher total reflectance compared to the periodic SL from

**ADVANCED
SCIENCE NEWS**

www.advancedsciencenews.com

**ADVANCED
OPTICAL
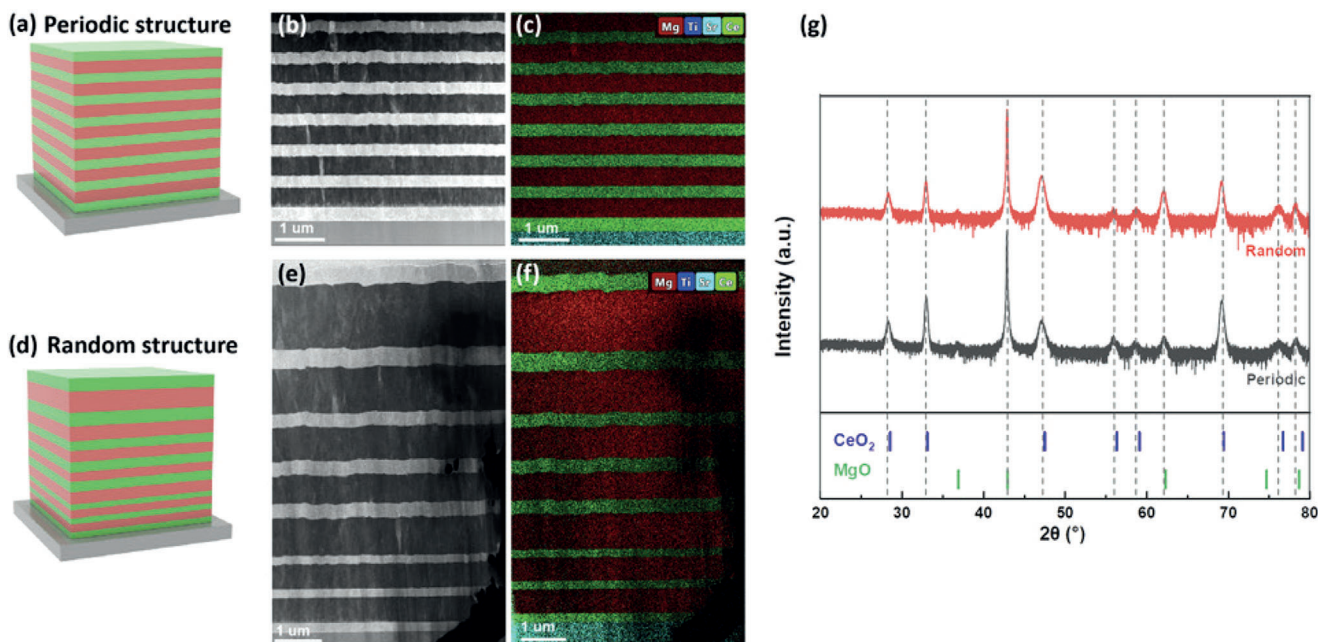MATERIALS**

www.advopticalmat.de

Figure 7. Fabrication and characterization of the multilayers: a) Model of the periodic multilayer, b) Transmission electron microscopy (TEM) image of the cross-section of fabricated periodic multilayer, c) Energy dispersive X-ray spectroscopy (EDS) of the periodic multilayer, d) Model of the random multilayer, e) TEM image of the cross-section of fabricated optimized RML, f) EDS of the fabricated optimized RML, g) X-ray diffraction spectra of the fabricated periodic and optimized RML.
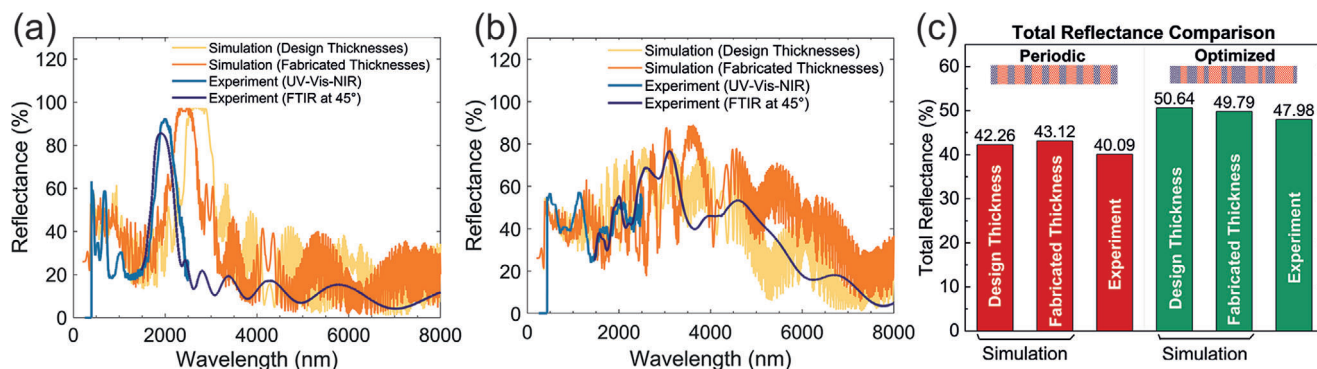

Figure 8. Comparison between the simulated spectral reflectance of the multilayer structure with design thicknesses and the experimentally measured spectral reflectance of the corresponding fabricated multilayer structure, for the a) periodic and b) random multilayer structures. The simulated spectral reflectance of each structure with the fabricated thicknesses is also plotted for both cases. c) Comparison of the total reflectance of periodic and optimized RML along with fabrication uncertainty.

both the simulated and measured data. In particular, we experimentally obtain a total reflectance of 47.98% in the RML structure, which is 8% higher than the 40.09% reflectance measured for the periodic SL. Such a large relative improvement of 20% (from $R = 40\%$ to $R = 48\%$), on a coating of only 5 µm thickness is significant for thermal barrier coating design. This provides an experimental demonstration of the success of our GA-based optimization process. The measured reflectance shows only 5% relative error to the designed reflectance of 50.64%.

We further analyze the causes of the error between designed and measured reflectances. There are fabrication uncertainties leading to deviation of layer thicknesses from the target, hence we compare the total simulated reflectances of the design thick-

ness and fabricated thickness structures. As expected, the highest reflectance is obtained from TMM simulation for the GA-optimized RML with ideal layer thicknesses, since it corresponds to an ideal simulation for an RML with perfectly optimized layer thicknesses. We achieve a total reflectance of 50.64%, compared to the TMM simulation on the periodic SL with ideal layer thicknesses that shows a 42.26% total reflectance. Interestingly, the layer thickness deviations in the fabricated structures causes opposite effects in the two cases, increasing the SL reflectance while reducing the GA-optimized RML reflectance. This is because, any addition of randomness in the periodic multilayer enhances the photon localization effect, while any deviations from the ideal thicknesses in the optimized RML structure takes it away from

the global maxima found by the GA and leads to a lower reflectance. This also clearly indicates that it is the randomness in layer thicknesses, not the larger total thickness, in the fabricated structure aperiodic multilayer that enhances the total reflectance. Therefore, we obtain a simulated total reflectance of 43.12% in periodic SL with fabricated thickness (1% higher) and 49.79% in the RML with fabricated thicknesses (1% lower). Such a small change indicates that the optimization is robust against fabrication uncertainty, which is a benefit of our system. The further differences between the simulated and measured reflectances using fabricated thicknesses may be attributed to other non-ideal effects not captured in the simulation, such as interface quality, surface roughness and center-to-edge thickness variation. Previous studies[41,42] have also shown that there is also uncertainty in the optical constants of the fabricated layers.

4. Conclusion

In summary, we demonstrate a machine learning (ML) based optimization method to discover CeO_2-MgO random multilayer (RML) structures with high reflectance for applications as high temperature thermal barrier coatings (TBCs). The transfer matrix method was used to evaluate the spectral reflectance of candidate multilayer structures. We first use a manual search to demonstrate the influence of RML design parameters on the reflectance, such as the total thickness, average layer thickness, and degree of randomness in layer thicknesses compared to a periodic superlattice (SL). For the periodic SLs of different total thicknesses from 1–50 μm, the presence of an optimum average layer thickness was noticed at which the total reflectance at $T = 1500K$ is maximized, due to the overlap of a high reflectance "stop band" within the spectral reflectance curve with the peak of the blackbody radiation spectrum. The influence of randomness in layer thicknesses was found to lead to a broadband increase in spectral reflectance due to the effect of photon localization. In order to efficiently scan the RML design space, a Genetic Algorithm (GA) based optimization framework was developed to identify high reflectance RML structures with total thicknesses of 5, 10, 20, and 30 μm. The optimized RML structures were found to have total reflectivities of 59%, 73%, 85%, and 90%, respectively, which translates to an enhancement of 22%, 20%, 20%, and 10% over the reflectance in randomly generated RMLs with same total thickness. Surprisingly, all our GA-optimized RML structures show the presence of an odd number of layers with a CeO_2 layer at either end, which deviates from the traditional way of designing binary superlattices with paired layers. This occurs because the unpaired CeO_2 layer in the optimized RMLs provide a greater contrast in refractive index with air, leading to a higher interface reflectance. We also calculate the field intensity distribution within the optimal and sub-optimal RML and reference SL structures to demonstrate the effect of photon localization. We then used Pulsed Laser Deposition to fabricate the optimized RML structure of 5 μm total thickness and a reference SL structure of same total thickness and average period. The fabricated structures showed clean interfaces, good crystallinity and stability at high temperatures, despite some deviation of layer thicknesses observed from the target thicknesses. This confirms the robustness of the machine learning approach. Optical reflectance measurements were carried out for both the fabricated structures.

The fabricated RML shows a total reflectance of 48%, which is 8% higher than that of the fabricated SL structure, thus demonstrating the success of our GA optimization framework. Our work demonstrates an efficient and general purpose method for performing ML-accelerated design optimization for target radiative properties of nanostructures, along with experimental validation of our simulation and optimization framework.

Conflict of Interest

The authors declare no conflict of interest.

Data Availability Statement

The data that support the findings of this study are available from the corresponding author upon reasonable request.

[1] M. Stiger, N. Yanar, M. Topping, F. Pettit, G. Meier, *Zeitschrift fur Metallkunde* **1999**, *90*, 1069.
[2] L. Chen, *Surf. Rev. Lett.* **2006**, *13*, 535.
[3] R. Vassen, X. Cao, F. Tietz, D. Basu, D. Stöver, *J. Am. Ceram. Soc.* **2000**, *83*, 2023.
[4] J. R. Nicholls, K. Lawson, A. Johnstone, D. Rickerby, in *Materials science forum*, vol. *369*, Trans Tech Publ, Stafa-Zurich, Switzerland **2001**, pp. 595–606.
[5] J. Wu, X. Wei, N. P. Padture, P. G. Klemens, M. Gell, E. García, P. Miranzo, M. I. Osendi, *J. Am. Ceram. Soc.* **2002**, *85*, 3031.
[6] D. Zhu, Y. L. Chen, R. A. Miller, *Ceram. Eng. Sci. Proc.* **2003**, *24*, 525.
[7] J. Wang, Y. Zhou, X. Chong, R. Zhou, J. Feng, *Ceram. Int.* **2016**, *42*, 13876.
[8] J. Wang, X. Chong, R. Zhou, J. Feng, *Scr. Mater.* **2017**, *126*, 24.
[9] R. Siegel, C. M. Spuckler, *Mater. Sci. Eng., A* **1998**, *245*, 150.
[10] J. I. Eldridge, C. M. Spuckler, K. W. Street, J. R. Markham, in 26th Annual Conference on Composites, Advanced Ceramics, Materials, and Structures: B: Ceramic Engineering and Science Proceedings, vol. *23*, John Wiley & Sons, Inc, Hoboken, NJ, USA **2002**, pp. 417–430.
[11] D. E. Wolfe, J. Singh, R. A. Miller, J. I. Eldridge, D.-M. Zhu, *Surf. Coat. Technol.* **2005**, *190*, 132.

**ADVANCED
SCIENCE NEWS**

www.advancedsciencenews.com

**ADVANCED
OPTICAL
MATERIALS**

www.advopticalmat.de

[12] H. Chen, Y. Liu, Y. Gao, S. Tao, H. Luo, *J. Am. Ceram. Soc.* **2010**, *93*, 1732.

[13] V. Stathopoulos, V. Sadykov, S. Pavlova, Y. Bespalko, Y. Fedorova, L. Bobrova, A. Salanov, A. Ishchenko, V. Stoyanovsky, T. Larina, et al., *Surf. Coat. Technol.* **2016**, *295*, 20.

[14] L. Swadźba, G. Moskal, B. Mendala, M. Hetmańczyk, *Arch. Metall. Mater.* **2008**, *53*, 945.

[15] C. Tekmen, I. Ozdemir, E. Celik, *Surf. Coat. Technol.* **2003**, *174*, 1101.

[16] M. J. Kelly, D. E. Wolfe, J. Singh, J. Eldridge, D.-M. Zhu, R. Miller, *Int. J. Appl. Ceram. Technol.* **2006**, *3*, 81.

[17] X. Huang, D. Wang, P. Patnaik, J. Singh, *Mater. Sci. Eng., A* **2007**, *460*, 101.

[18] W. Ge, C. Zhao, B. Wang, *Int. J. Heat Mass Transfer* **2019**, *134*, 101.

[19] S. Ju, T. Shiga, L. Feng, Z. Hou, K. Tsuda, J. Shiomi, *Phys. Rev. X* **2017**, *7*, 021024.

[20] H. Yang, Z. Zhang, J. Zhang, X. C. Zeng, *Nanoscale* **2018**, *10*, 19092.

[21] H. Wei, S. Zhao, Q. Rong, H. Bao, *Int. J. Heat Mass Transfer* **2018**, *127*, 908.

[22] P. R. Chowdhury, C. Reynolds, A. Garrett, T. Feng, S. P. Adiga, X. Ruan, *Nano Energy* **2020**, *69*, 104428.

[23] P. Chakraborty, Y. Liu, T. Ma, X. Guo, L. Cao, R. Hu, Y. Wang, *ACS Appl. Mater. Interfaces* **2020**, *12*, 8795.

[24] H. Wei, H. Bao, X. Ruan, *Nano Energy* **2020**, *71*, 104619.

[25] P. Roy Chowdhury, X. Ruan, *npj Comput. Mater.* **2022**, *8*, 1.

[26] Y. Wang, H. Huang, X. Ruan, *Phys. Rev. B* **2014**, *90*, 165406.

[27] Y. Shi, W. Li, A. Raman, S. Fan, *ACS Photonics* **2017**, *5*, 684.

[28] A. Sakurai, K. Yada, T. Simomura, S. Ju, M. Kashiwagi, H. Okada, T. Nagao, K. Tsuda, J. Shiomi, *ACS Cent. Sci.* **2019**, *5*, 319.

[29] J. Guo, S. Ju, J. Shiomi, *Opt. Lett.* **2020**, *45*, 343.

[30] D. Chae, M. Kim, P.-H. Jung, S. Son, J. Seo, Y. Liu, B. J. Lee, H. Lee, *ACS Appl. Mater. Interfaces* **2020**, *12*, 8073.

[31] M. Kim, J. Seo, S. Yoon, H. Lee, J. Lee, B. J. Lee, *J. Quant. Spectrosc. Radiat. Transfer* **2021**, *260*, 107475.

[32] S. Kim, W. Shang, S. Moon, T. Pastega, E. Lee, T. Luo, *ACS Energy Lett.* **2022**, *7*, 4134.

[33] R. E. Stephens, I. H. Malitson, *J. Res. Natl. Bur. Stand.* **1952**, *49*, 249.

[34] S. Guo, H. Arwin, S. Jacobsen, K. Järrendahl, U. Helmersson, *J. Appl. Phys.* **1995**, *77*, 5369.

[35] P. W. Anderson, *Phys. Rev.* **1958**, *109*, 1492.

[36] A. McGurn, K. Christensen, F. Mueller, A. Maradudin, *Phys. Rev. B* **1993**, *47*, 13120.

[37] M. Sigalas, C. Soukoulis, *Phys. Rev. B* **1995**, *51*, 2780.

[38] B. Van Tiggelen, A. Lagendijk, D. Wiersma, *Phys. Rev. Lett.* **2000**, *84*, 4333.

[39] A. Lenert, D. M. Bierman, Y. Nam, W. R. Chan, I. Celanović, M. Soljačić, E. N. Wang, *Nat. Nanotechnol.* **2014**, *9*, 126.

[40] Y. S. Huang, C. C. Chang, J. W. Lee, Y. C. Lee, C. C. Huang, Z. K. Wun, K. K. Tiong, *Phys. Scr.* **2013**, *T157*, 014034.

[41] C. Lee, D. Kortge, J. Zhu, J. Song, H. Wang, X. Ruan, P. Bermel, *J. Opt.* **2023**, *25*, 085901.

[42] Z. Han, C. Lee, J. Song, H. Wang, P. Bermel, X. Ruan, *Phys. Rev. B* **2023**, *107*, L201202.

2300610 (13 of 13)